



Optics Letters

Self validating Mueller matrix Micro–Mesoscope (SAMMM) for the characterization of biological media

ILYAS SAYTASHEV,^{1,2}  SUDIPTA SAHA,² JOSEPH CHUE-SANG,² PEDRO LOPEZ,¹ MEGAN LAUGHREY,¹ AND JESSICA C. RAMELLA-ROMAN^{1,2,*}

¹Department of Ophthalmology, Herbert Wertheim College of Medicine, Florida International University, 11200 SW 8th Street, Miami, Florida 33199, USA

²Department of Biomedical Engineering, College of Engineering and Computing, Florida International University, 10555 West Flagler Street, Miami, Florida 33174, USA

*Corresponding author: jramella@fiu.edu

Received 20 January 2020; revised 20 February 2020; accepted 21 February 2020; posted 13 March 2020 (Doc. ID 387747); published 7 April 2020

Reflectance Mueller matrix (MM) polarimetry is being used to characterize biological media in multiple clinical applications. The origin of the reflectance polarimetric data is often unclear due to the impact of multiple scattering and tissue heterogeneity. We have developed a new, to the best of our knowledge, multimodal imaging technique combining MM reflectance, MM digital confocal imaging, and co-registered nonlinear microscopy techniques. The instrument unveils the origin of reflectance polarimetric signature in terms of confocal reflectance data. The reconstructed reflected MM demonstrates the capability of our method to provide depth-resolved 3D polarization response from complex biological media in terms of depolarization, retardance, and orientation parameters. © 2020 Optical Society of America

<https://doi.org/10.1364/OL.387747>

Polarization-based imaging techniques are becoming of widespread use due to their unique ability to target structural components in both excised and live biological tissue. Mueller matrix (MM) polarimetry (MMP) has been used extensively in the determination of orientation and retardance of fibrous tissues due to its ability to measure birefringence [1,2]. In parallel to preclinical and clinical work, multiple studies have been conducted to better understand how polarized light travels through and interacts with biological media [2]. In the past, polarized light transfer modeling has been approached through stochastic models and from a wave equation standpoint [3–6]. Currently, fundamental experimental work utilizing standards [7–10] have shown how different incident polarization states are maintained while travelling into multi-scattering media. At the same time, different ways of decomposing the 4×4 MM demonstrate the important need to simplify and access the basic medium polarimetry parameters, namely, diattenuation, retardance, and depolarization [7,11,12]. As physicians and scientists move these polarization modalities into complex biological environments, our understanding of the collected

signal is limited by both the lack of well-characterized phantoms [13] mimicking such complexity and lack of mathematical models that take such complexity into account. This Letter and the instrumentation at its core address in part this interesting unsolved problem. We have developed an instrument that combines two polarization imaging techniques, MM reflectance and MM confocal polarimetry [14], and integrated these modalities into a nonlinear microscope [15,16]. A system that combines confocal MM polarimetry and nonlinear microscopy has previously been proposed by Okoro *et al.* [17]. In their work, the confocal MM image was related to the co-registered nonlinear data and was even used to pattern the MM images for better analysis. Similarly, Bancelin *et al.* demonstrated through two independent imaging systems that second-harmonic generation (SHG) microscopy and transmission MM microscopy provides comparable information about the arrangement of anisotropic structures [18]. Our intent here is different, yet builds on these approaches—we have an added capability which allows for the collection of the back-reflected MM image, together with the depth-dependent confocal MM and nonlinear images. The back-reflected MM images contain the signals reflected from the total volume (bulk) of the sample. Using our system, we can study the origin of the back-reflected MM, which is most commonly used in clinical applications [13,19,20]. Thus, we can improve our understanding of the cumulative effect of photons traveling through multiply scattering media on the bulk reflected depolarization, retardance, and diattenuation.

The combined nonlinear and MMP imaging setup is shown in Fig. 1. A pre-compensated beam from a broadband femtosecond laser (Element 600, Femtolasers, Vienna, Austria) is directed into a home-built laser scanning microscope, where it is focused into a specimen through a long working distance objective (Mitutoyo $5 \times /0.14$ NA). Reflected light at a fundamental wavelength range (700–900 nm) is separated from epi-detected two-photon excitation fluorescence (TPEF) and SHG by a short-pass dichroic mirror (650 nm, Chroma Technology Corp., Bellows Falls, VT) and directed to an output port by a

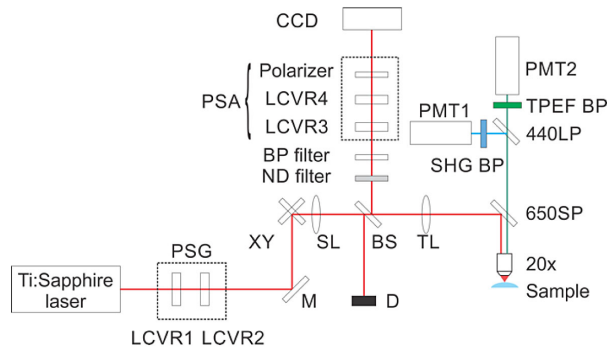


Fig. 1. Schematic diagram of a co-registered nonlinear and MMP laser scanning microscope.

10:90 non-polarizing beam splitter placed between scanning and tube lenses of a microscope. The optical signal through the beam splitter is filtered with a bandpass filter (780 nm central wavelength, 10 nm FWHM) and collected by a (CMOS) camera (PCO-Edge 5.5, PCO AG, Kelheim, Germany) which is placed at the conjugate imaging plane. The CMOS sensor active area is $5.7 \times 4.28 \text{ mm}^2$ with a physical pixel size of $2.2 \text{ }\mu\text{m}$. A 7×7 binning is applied to a camera increasing the frame rate to 120 fps and reducing the resolution to $368 \times 276 \text{ pixels}^2$ with an effective pixel size of $15.4 \text{ }\mu\text{m}$. The nonlinear SHG and TPEF optical signals are separated using a second dichroic mirror (440 nm, Chroma Technology Corp., Bellows Falls, VT) and detected by respective photosensor (H10720-210, Hamamatsu Photonics K.K., Shizuoka, Japan) with suitable bandpass filters (Semrock 400/30 nm and 500/24 nm, IDEX Health & Science LLC, Rochester, NY).

MM polarimetry imaging is enabled by an addition of a polarization state generator (PSG) at the microscope input, and a polarization state analyzer (PSA) before the camera in the linear reflectance arm. Both the PSA and PSG consist of a pair of liquid crystal variable retarders (LCVRs, Meadowlark Optics, Frederick, CO) and a linear polarizer (LPNIR100, Thorlabs Inc., Newton, NJ) oriented parallel to the reference plane (optical bench). We omit the linear polarizer in the PSG, since the laser itself is polarized parallel to the reference plane. All four LCVRs are operated by a D3040 USB controller (Meadowlark Optics, Frederick, CO). The laser beam is scanned across the sample with a pair of galvanometer mirrors (GVS102, Thorlabs Inc., Newton, NJ). For each scanning position, the back-propagated nonlinear signal is collected by a pair of photo multiplier tube detectors and a DAQ board (PCIe-6351, National Instruments, Austin, TX) simultaneously.

During acquisition, the camera records one frame for each laser position containing a reflection from the imaged sample. To remove the out-of-focus signal, our software defines active pixels on a camera according to a pre-calibrated laser beam scanning position and the virtual pinhole size d [21]; the adjustable confocal parameter d is set to five pixels leading to approximately $10 \text{ }\mu\text{m}$ axial resolution. Pixel intensities inside the defined mask of each acquired frame are ultimately added to the output image. An intensity image for back-reflected MM is created by adding all acquired camera frames without applying a virtual pinhole. After laser scans through the sample by a predetermined pattern (trigonal scan $128 \times 128 \text{ pixels}^2$), four output images are reconstructed: TPEF, SHG, confocal

reflectance, and back-reflected MM for each PSG and PSA state. The resulting output on each imaging plane is a set of microscopic images: two are obtained from nonlinear channels, and 24 are confocal intensity images from a camera. The pre-processing routine only applies an averaging filter with a size of two pixels for the input images to reduce the noise.

The calibration of the MMP system is done using an external calibrated polarimeter (Thorlabs Inc., Newton, NJ). An optical filter (780, 10 nm FWHM) is temporarily placed in the beam path before the LCVRs of the PSG to restrict the laser bandwidth during calibration, and then removed once the calibration procedure is finished. The generated polarization states at the focal plane of the objective are $[1 \ 0.43 \ 0.66 \ 0.61]^T$, $[1 \ -0.97 \ 0.15 \ 0.21]^T$, $[1 \ -0.52 \ -0.75 \ -0.40]^T$, $[1 \ 0.50 \ -0.14 \ 0.85]^T$, $[1 \ 0.28 \ 0.87 \ 0.40]^T$, and $[1 \ 0.80 \ 0.09 \ -0.60]^T$ with the largest RMS error of 0.4%. Similarly, the measured four output Stokes vectors are $[1 \ 0.33 \ 0.76 \ -0.49]^T$, $[1 \ 0.23 \ -0.58 \ 0.77]^T$, $[1 \ -0.88 \ 0.52 \ 0.40]^T$, and $[1 \ 0.26 \ -0.76 \ 0.68]^T$ with a 3% RMS error. Using these states, a reflectance intensities matrix is obtained and after few algebraic manipulations the MM can be constructed [2,14]. Once the LCVRs of the PSG and PSA are set to the calibrated values, the system's MM M_{sys} is measured using a mirror and placed at the focal plane of an objective.

The decomposition of the sample's MM M_s as proposed by Lu–Chipman [11], yields three canonical matrices accounting for material depolarization M_Δ : retardance, optical activity M_R , and diattenuation M_D : $M_s = M_\Delta M_R M_D$. Further, linear retardance and orientation of a fast optical axis can be calculated from a retardance matrix M_R . MM retrieval and decomposition at each pixel results in images of depolarization, orientation, and linear retardance maps. MM calculation, decomposition, and visualization are performed using MATLAB. Depth-resolved data are reconstructed as planes in 3D volume for all calculated polarization parameters, as well as nonlinear images to demonstrate the dynamic change with depth. Hence, our Self-validating Mueller matrix Micro-Mesoscope (SAMMM) can be used to confirm if the changes in the MM of the depth-dependent data are due to a birefringence or other type of interaction. To demonstrate the system capability, we imaged two types of model samples: (1) an optical phantom made of titanium dioxide showing only depolarization effect and (2) a nylon fiber placed in a highly scattering medium (milk) having both depolarization and retardance effects.

The optical phantom consisting of titanium dioxide was used for recording both the confocal and back-reflected MM images. In Fig. 2(a), we show the variation of average polarization-independent reflectance intensity (given by M_{11}) with depth from the surface of the phantom from a region of the optical phantom. The corresponding depolarization coefficients are shown in Fig. 2(b). The variation of these parameters with different confocal pinhole sizes is shown by 1×1 , 3×3 , 5×5 and 7×7 . Here 1×1 , 3×3 , 5×5 and 7×7 represent pinholes with an effective radius of 16, 48, 80, and 112 μm , respectively. As expected, with increasing depth, depolarization increases. Increasing pinhole size yields higher M_{11} values; however, the depolarization does not vary significantly. For back reflectance, the recorded M_{11} and the corresponding depolarization remain the same for all depths. It is important to note that the depolarization in a back-reflected MM is higher

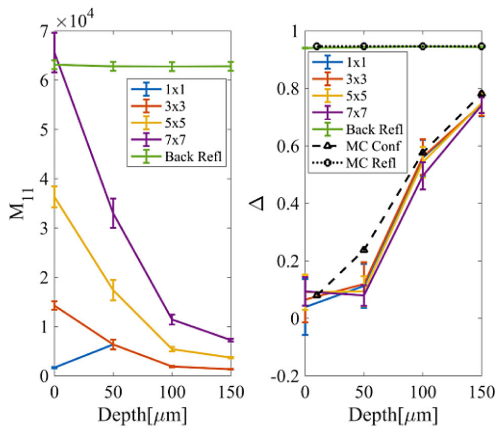


Fig. 2. (a) Polarization-independent unnormalized (average) intensity M_{11} from a region of titanium dioxide phantom and (b) the depolarization coefficient for different pinhole size in a confocal MM and back-reflected MM geometry as a function of distance from the surface of the phantom for one region of interest. The Monte Carlo simulated depolarization coefficients for both the confocal (MC Conf) and back-reflected MM (MC Refl) are also shown by black dashed and dotted lines, respectively.

than the depolarization in confocal MM measurements, but the values asymptotically converge. We utilize a previously developed Monte Carlo model of polarized light transfer to model the interaction of titanium dioxide phantom with polarized light for both a back-reflected MM and confocal Mueller Matrix imaging. A confocal pinhole is added to the program following the approach by Tanbakuchi *et al.* [22]. Model parameters are $\mu_a = 0.33 \text{ cm}^{-1}$, $\mu_s = 62.5 \text{ cm}^{-1}$ average particle radius = $0.135 \text{ }\mu\text{m}$, $n = 2.5$ for the particle and 1.54 medium, following the report of Firbank *et al.* [23] with the laser wavelength of $0.78 \text{ }\mu\text{m}$. 10 million photons are used in the simulation. Figure 2(b) shows good agreement of Monte Carlo simulation results (black symbols) with the experimental findings (colored symbols).

In a second experiment, we imaged a nylon fiber submerged in a milk solution. The choice of nylon fiber is motivated by the fact that it is known to possess high birefringence properties, while the milk is highly scattering and has been used to mimic biological media. The idea is to show how our method can capture/differentiate the actual polarization properties arising from the local environmental anisotropies. A total of 41 planes were imaged with a step size of $10 \text{ }\mu\text{m}$ starting from the surface of the sample. In Fig. 3, we have shown the SHG, M_{11} , depolarization, and linear retardance at different depths from this sample. At the beginning, the imaging plane does not include the fiber; we only observe the signal from the milk solution. However, after about $80 \text{ }\mu\text{m}$ from the surface, we start seeing the images of the fiber in both SHG (column 1) and M_{11} (column 2) images. The corresponding depolarization and linear retardance are shown in columns 3 and 4, respectively.

When the imaging plane meets the fiber, we notice that the depolarization and linear retardance of the fiber are higher than the surrounding milk. After the imaging plane crosses the fiber, we no longer see the image of the fiber in SHG and M_{11} images, while the corresponding depolarization and retardance images maintain a memory of the interaction as expected. This is true for all subsequent layers, although interaction with the milk

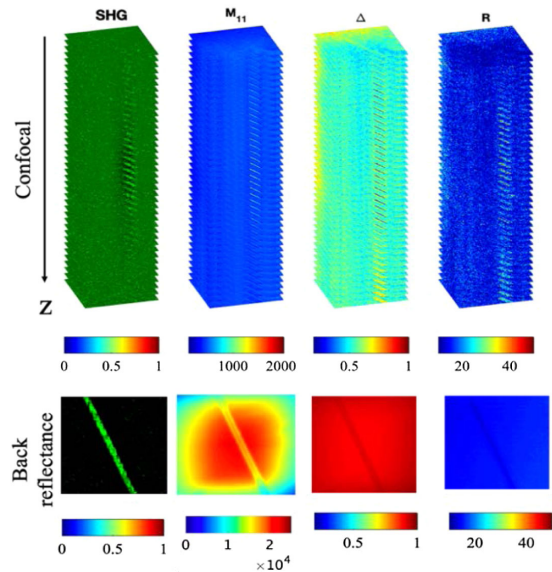


Fig. 3. Top panel, depth-resolved SHG, confocal M_{11} , depolarization, and linear retardance (degrees) images of nylon fiber placed in a milk solution; bottom panel, the corresponding quantities in back reflectance. The SHG signal is square-rooted for visualization purposes. The size of the imaging area is $240 \text{ }\mu\text{m} \times 240 \text{ }\mu\text{m}$.

does distort the subsequent images. The bottom row shows the back-reflected SHG, M_{11} , depolarization, and linear retardance from the entire sample.

Numerical analysis of the data for all layers shows that the effect of the polarized light on the birefringent nylon fiber is position dependent (Fig. 4). To illustrate this, depolarization from two regions of interest—at the central portion and on the side of a nylon fiber—is plotted against the imaging depth. The imaging layer containing the nylon fiber can be clearly visualized through the SHG data (dotted black line); the confocal depolarization is observed at the center of the fiber decreases, as we approach the imaging layer with a nylon fiber possibly due to a heightened specular reflectance, while the opposite is true when we analyze depolarization on the side region of the fiber. In back reflectance, the depolarization does not change significantly, as the objective moves closer to the sample, but the results on the depolarization are still position dependent.

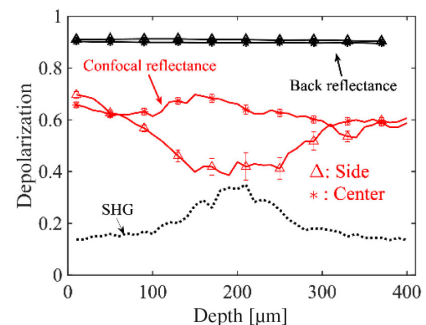


Fig. 4. Depolarization in confocal (red) and back reflectance (black). The SHG signal (black dotted line) demonstrates the presence of a nylon fiber in the middle of a depth scan. The legends “Side” (Δ) and “Center” ($*$) refer to the region at the central and side portions of the nylon fiber in both confocal and back reflectance data.

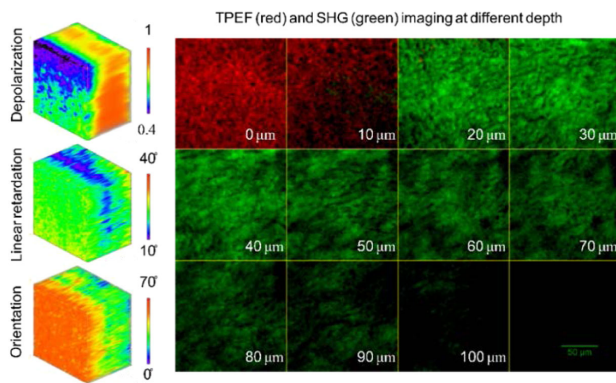


Fig. 5. Full-depth two-photon and confocal MMP imaging of an unstained rat cornea. A $120\ \mu\text{m} \times \mu\text{m}$ imaging area was taken at the center of a cornea.

Values selected from the center of the fiber have higher retardance and lower depolarization than the values collected on the side, (a student T test conducted on the data on the center of the fiber and on the side shows a p value of 0.02 on average).

Finally, we show an application of our system to biological media. A rat cornea was stained with DAPI (Fig. 5), marking the presence of epithelial cells and keratocytes. Tightly packed epithelial layer cells slowly depolarize light; this effect increases as the image plane crosses the stromal anterior layer and exhibits higher values reaching the posterior stroma. The presence of both TPEF and SHG signals in a $0\ \mu\text{m}$ imaging layer suggests that the imaging plane was at the Bowman's layer (superficial layer between epithelium and the stroma in the cornea), therefore containing signals from epithelium cells (TPEF) and stromal collagen (SHG). A clear separation among epithelium and stromal layers is noticeable in the linear retardation and orientation volumes.

In conclusion, our SAMMM system can provide depth-resolved confocal and back-reflected MM imagery, as well as co-registered SHG and TPEF for validation. We have begun exploring how polarized light travels through a scattering media and depolarizes; we have also shown that the depolarization and retardance caused by a birefringent fiber is influenced by its shape and location. The initial results on an excised rat cornea demonstrate clear depth-resolved regions of polarization sensitive interaction. All of this brings into question current decomposition methods, particularly for back-reflected MM images; these methods cannot account for discrete transitions such as the ones shown in Figs. 3 and 5. Our future work will focus on this issue evaluating the error associated with the decomposition methods in layered biological media.

Funding. National Science Foundation (DMR 1548924); Herbert Wertheim College of Medicine, Florida International University (H. and N. Wertheim Professorship Endowment); NSF (NSF.EEC-1648451).

Acknowledgment. The authors are grateful to Jefferson Gomes for cornea sample preparation.

Disclosures. The authors declare no conflicts of interest.

REFERENCES

- V. V. Tuchin, *J. Biomed. Opt.* **21**, 071114 (2016).
- N. Ghosh and I. A. Vitkin, *J. Biomed. Opt.* **16**, 110801 (2011).
- M. R. Antonelli, A. Pierangelo, T. Novikova, P. Validire, A. Benali, B. Gayet, and A. De Martino, *Opt. Express* **18**, 10200 (2010).
- P. Ghassemi, L. T. Moffatt, J. W. Shupp, and J. C. Ramella-Roman, *J. Biophotonics* **9**, 100 (2016).
- J. Ramella-Roman, S. Prah, and S. Jacques, *Opt. Express* **13**, 4420 (2005).
- T. Yun, N. Zeng, W. Li, D. Li, X. Jiang, and H. Ma, *Opt. Express* **17**, 16590 (2009).
- M. Sun, H. He, N. Zeng, E. Du, Y. Guo, S. Liu, J. Wu, Y. He, and H. Ma, *Biomed. Opt. Express* **5**, 4223 (2014).
- T. S. Eliasdottir, D. Bragason, S. H. Hardarson, G. Kristjansdottir, and E. Stefansson, *Graefes' archive for clinical and experimental ophthalmology = Albrecht von Graefes Archiv fur klinische und experimentelle Ophthalmologie* (2015).
- S. Rehn, A. Planat-Chretien, M. Berger, J. M. Dinten, C. Deumie, and A. da Silva, *J. Biomed. Opt.* **18**, 16007 (2013).
- A. Da Silva, C. Deumié, and I. Vanzetta, *Biomed. Opt. Express* **3**, 2907 (2012).
- S. Y. Lu and R. A. Chipman, *J. Opt. Soc. Am. A* **13**, 1106 (1996).
- R. Ossikovski, A. De Martino, and S. Guyot, *Opt. Lett.* **32**, 689 (2007).
- J. Chue-Sang, M. Gonzalez, A. Pierre, M. Laughrey, I. Saytashev, T. Novikova, and J. C. Ramella-Roman, *J. Biomed. Opt.* **24**, 1 (2019).
- D. Lara and C. Dainty, *Opt. Lett.* **30**, 2879 (2005).
- J. M. Bueno, F. J. Ávila, and P. Artal, *Microsc. Anal.* (2016).
- W. Denk, J. H. Strickler, and W. W. Webb, *Science* **248**, 73 (1990).
- C. Okoro and K. C. Toussaint, *J. Biomed. Opt.* **22**, 086007 (2017).
- S. Bancelin, A. Nazac, B. H. Ibrahim, P. Dokladal, E. Decenciére, B. Teig, H. Haddad, H. Fernandez, M. C. Schanne-Klein, and A. De Martino, *Opt. Express* **22**, 22561 (2014).
- S. Alali and A. Vitkin, *J. Biomed. Opt.* **20**, 061104 (2015).
- J. Chue-Sang, N. Holness, M. Gonzalez, J. Greaves, I. Saytashev, S. Stoff, A. Gandjbakhche, V. V. Chernomordik, G. Burkett, and J. C. Ramella-Roman, *J. Biomed. Opt.* **23**, 121605 (2018).
- E. Sanchez-Ortiga, G. Saavedra, M. Martinez-Corral, A. Doblas, and A. Calatayud, *10th Euro-American Workshop on Information Optics* (2011).
- A. A. Tanbakuchi, J. A. Udovich, A. R. Rouse, K. D. Hatch, and A. F. Gmitro, *Am. J. Obstet. Gynecol.* **202**, 90.e1 (2010).
- M. Firbank, M. Oda, and D. T. Delpy, *Phys. Med. Biol.* **40**, 955 (1995).